Table 2

Diagnostic Value of Elastographic Criteria for Metastatic Lymph Nodes

Imaging Examination and Criterion	Sensitivity (%)	Specificity (%)	Positive Predictive Value (%)	Negative Predictive Value (%)	Overall Accuracy (%)
B-Mode US					
Short axis diameter > 8 mm	47 (34, 59)	79 (70, 88)	62 (48, 76)	67 (57, 76)	65 (57, 73)
Short-to-long-axis diameter ratio > 0.5	75 (64, 86)	81 (73, 90)	75 (64, 86)	81 (73, 90)	79 (72, 85)
Absent hilum	72 (60, 83)	54 (44, 65)	54 (43, 65)	72 (61, 83)	62 (54, 70)
Abnormal echogenicity	58 (46, 71)	91 (85, 97)	83 (72, 95)	75 (66, 83)	77 (70, 84)
Calcifications	3 (−1, 8)	100 (100, 100)	100 (100, 100)	58 (50, 66)	59 (51, 67)
Peripheral vascularity at power Doppler US	47 (34, 59)	99 (96, 101)	97 (90, 103)	71 (63, 80)	77 (70, 84)
Sonoelastography					
Lymph node partially or very visible	67 (55, 79)	93 (87, 98)	87 (77, 97)	79 (71, 87)	82 (75, 88)
Lymph node darker than surrounding muscles	63 (51, 76)	95 (90, 99)	91 (82, 99)	78 (70, 86)	82 (75, 88)
Regular or moderately irregular margin	35 (23, 47)	95 (90, 100)	84 (70, 98)	66 (58, 75)	70 (62, 77)
>50% of Margin border distinct	48 (36, 61)	73 (63, 83)	57 (43, 70)	66 (56, 75)	62 (54, 70)
Strain index >1.5	85 (76, 94)	98 (94, 101)	96 (91, 101)	90 (83, 96)	92 (88, 97)

Note.—Numbers in parentheses are 95% confidence intervals (CIs).

lymph nodes. A multivariate analysis was performed by using the generalized estimating equation method to select the variables (ie, examined US and elastographic criteria) that were independently associated with lymph node metastasis (17,18). This is a repeated-measures analysis for correlated dichotomous outcomes (metastatic lymph nodes) and a set of covariates (examined US and elastographic criteria). The generalized estimating equation method was used to adjust the intracorrelation effect for patients who had multiple measurements. Each variable had a binary value (greater than and less than the selected cutoff value).

The model used was selected on the basis of the Akaike information criterion and the Schwarz Bayesian criterion. For each criterion examined, the sensitivity, specificity, positive and negative predictive values, and overall accuracy in the differentiation between benign and metastatic lymph nodes were calculated. Quantitative data are presented as means ± 1 standard deviation. $P < .05$ indicated statistical significance. Post hoc power analysis involving the use of the two-sided Fisher exact test for binomial distribution was performed to determine whether the resultant sample size was of sufficient magnitude to support confidence in the outcome results (19). The statistical analyses were performed by using a statistical software package (StatView, version 5.0; SAS Institute, Cary, NC).

Results

Patients

At histologic analysis, 32 (74%) patients (14 men, 18 women; mean age, 59 years ± 11) were found to have papillary thyroid cancer, six (14%) (three men, three women; mean age, 50 years ± 12) were found to have follicular thyroid adenoma, and five (7%) (all men; mean age, 75 years ± 4) were found to have squamous cell cancer of the hypopharynx. The patients with hypopharyngeal cancer were significantly older than those with thyroid cancer ($P < .01$).

Lymph Nodes

A total of 141 peripheral neck lymph nodes (60 [43%] metastatic, 81 [57%] metastasis free) were examined. Metastasis from papillary thyroid cancer was histologically diagnosed in 39 nodes (28%), and metastasis from hypopharyngeal squamous cell cancer was histologically diagnosed in 21 (15%) nodes. Seventeen of the 43 patients (11 men, six women) had metastatic lymph nodes: Five patients had one metastatic lymph node each; four patients, two each; three patients, three each; two patients, four each; two patients, five each; and one patient, six each.

Nineteen patients (seven men, 12 women) had benign lymph nodes. Of these 19 patients, three had one benign lymph node each; five, two benign nodes each; four, three benign nodes each; three, five benign nodes each; three, six benign nodes each; and one, eight benign nodes each.

Seven patients (four men, three women) had both metastatic and metastasis-free (benign) lymph nodes. Of these seven patients, three had one metastatic and one benign lymph node; one patient, one metastatic and two benign nodes; one patient, one metastatic and five benign nodes; one patient, three metastatic and two benign nodes; and one patient, six metastatic and three benign nodes.

B-Mode US

There was no significant difference in the gray-scale US or elastographic lymph node characteristics between the patients with thyroid abnormalities and those with hypopharyngeal abnormalities. The characteristics of the examined lymph nodes are listed in Table 1,

and the diagnostic accuracy of each of the features tested is detailed in Table 2.

There was a significant difference in short-axis diameter between the metastatic (9.1 mm ± 5.8; 95% CI: 7.6 mm, 10.6 mm) and benign (6.6 mm ± 3.4; 95% CI: 5.8 mm, 7.4 mm) lymph nodes ($P < .01$). Twenty-one percent of the benign lymph nodes were larger than 8 mm, whereas 47% of the metastatic nodes were larger than 8 mm ($P < .01$). Other tested cutoff values of lymph node short-axis diameter (ie, 5 and 10 mm) enabled less accurate distinction between the benign and metastatic nodes. Marked improvement in diagnostic accuracy was achieved with use of the short-to-long-axis diameter ratio criteria: 75% of the metastatic lymph nodes versus 18% of the benign nodes showed a diameter ratio greater than 0.5 ($P < .01$). No further improvement in overall diagnostic accuracy was achieved with the other tested short-to-long-axis diameter ratio cutoff values (ie, 0.4 or 0.6). A hyperechoic hilum was absent in 72% of the metastatic and 46% of the benign lymph nodes ($P < .01$). With respect to echogenicity, 58% of the metastatic lymph nodes (nine [15%] hyperechoic, 26 [43%] hypoechoic) versus 9% of the benign nodes (two [2%] hyperechoic, five [6%] hypoechoic) ($P < .01$) showed abnormal echogenicity. Microcalcifications were rare findings in our study: They were observed exclusively in patients with metastatic lymph nodes but were diagnosed in only two (3%) of the examined nodes.

Figure 2

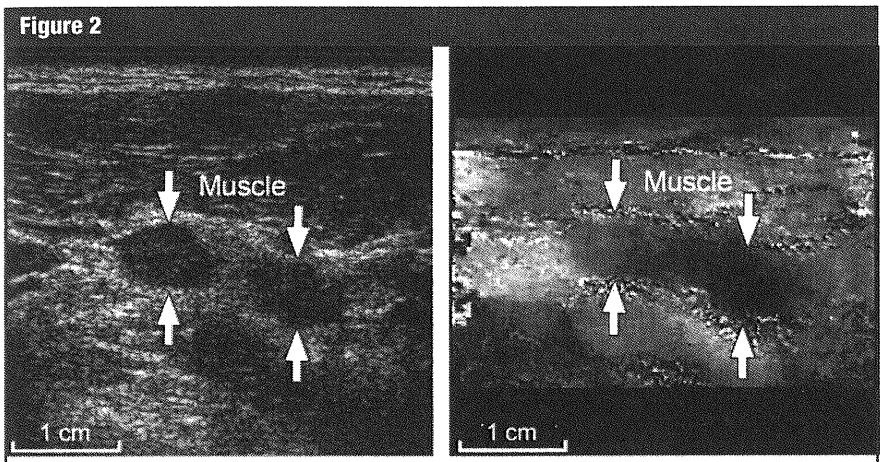

a. b.

Figure 2: Metastatic lymph nodes. **(a)** Gray-scale sonogram obtained in 64-year-old man with papillary thyroid cancer shows two hypoechoic metastatic lymph nodes (arrows) with a short-axis diameter of 6 mm, a short-to-long-axis diameter ratio greater than 0.5, and an absent hyperechoic hilum. **(b)** On corresponding US elastogram, lymph nodes (arrows) are very visible, are substantially darker than surrounding muscle, and have irregular and moderately distinct borders. Strain indexes are 2.5 and 7.8 for the right and left nodes, respectively.

Figure 3

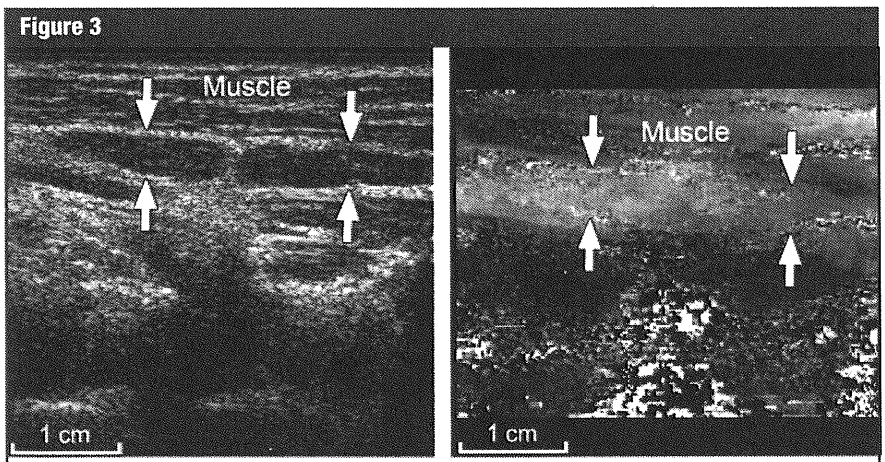

a. b.

Figure 3: Benign lymph nodes. **(a)** Gray-scale sonogram obtained in 48-year-old woman with follicular adenoma of thyroid gland shows a chain of benign lymph nodes (arrows) with a short-axis diameter of 5 mm and a short-to-long-axis diameter ratio smaller than 0.5. **(b)** On corresponding US elastogram, the lymph nodes (arrows) are partially visible and brighter than surrounding muscle and have irregular and somewhat distinct borders. Strain indexes are 0.3 and 0.7 for the right and left nodes, respectively.

Power Doppler US

Performing power Doppler US did not substantially improve the diagnostic accuracy of the US criteria for metastatic lymph nodes. Although only one (1%) benign lymph node had peripheral vascularity, this feature was observed in less that half (47%) of the metastatic lymph nodes ($P < .01$).

Sonoelastography

The majority (93%) of the metastatic lymph nodes (Fig 2) were very or partially visible on US elastograms and had a visualization score greater than 2. This finding was observed in 33% ($P < .01$) of the benign lymph nodes (Fig 3). Although the majority of the metastatic lymph nodes were visible on US elastograms, only 63% of them were substantially darker (ie, stiffer) than the surrounding tissues and had a relative brightness index lower than or equal to 2. Thirty-seven percent of the metastatic lymph nodes, as well as 95% of the benign nodes, were slightly darker, brighter, or the same in brightness compared with the surrounding muscles.

The diagnostic accuracy of lymph node margin evaluation was low in

terms of both regularity and definition. Although 95% of the benign nodes had irregular margins (regularity index < 2) and 73% of them had indistinct borders (margin definition index < 2), these same findings were observed in 65% and 52% of the metastatic lymph nodes, respectively.

In contrast, the diagnostic accuracy of the muscle-to–lymph node strain index was high. There was a significant difference in mean strain index between the benign and metastatic lymph nodes: 0.8 ± 0.5 (95% CI: 0.7, 0.9) versus 4.4 ± 3.6 (95% CI: 3.5, 5.3), respectively ($P < .01$). Among the numerous cutoff values tested, the strain index cutoff value of 1.5 enabled the best distinction between metastatic and benign lymph nodes. The majority (98%) of the benign lymph nodes were less than 1.5 times stiffer than the surrounding muscles; however, 85% of the metastatic lymph nodes were more than 1.5 times stiffer than the surrounding muscles ($P < .01$). When the diagnostic accuracy of a strain index greater than 1.5 was calculated, results showed that this criterion had 85% sensitivity, 98% specificity, a 96% positive predictive value, a 90% negative predictive value, and the highest overall accuracy (92%) of all the diagnostic criteria examined. The false-negative results obtained with this criterion included metastatic lymph nodes that were less than 1.5 times stiffer than the surrounding muscles owing to incomplete replacement of normal lymphoid tissues by malignant cells in six lymph nodes (Fig 4) and to central necrosis in three lymph nodes (Fig 5).

We confirmed our findings by using multivariate generalized estimating equation analysis. This analysis revealed that of all the examined criteria, only a short-to-long-axis diameter ratio greater than 0.5 (95% CI: 1.7, 16.3; $P < .01$), the absence of a hyperechoic hilum (95% CI: 2.0, 9.0; $P < .01$), peripheral vascularization (95% CI: 1.4, 24.5; $P < .05$), and a strain index greater than 1.5 (95% CI: 1.7, 18.6; $P < .01$) were significantly and independently associated with metastatic disease.

Figure 4

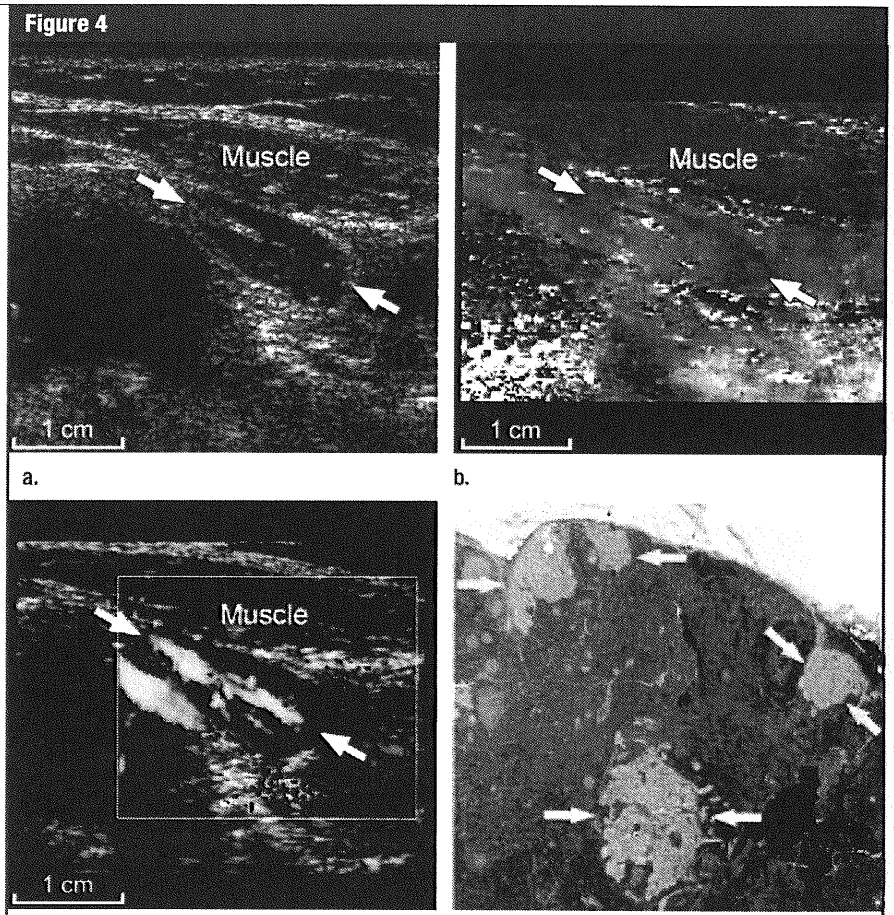

Figure 4: Metastatic lymph node with incomplete metastatic involvement. **(a)** Gray-scale sonogram obtained in 53-year-old man with papillary thyroid cancer shows metastatic lymph node (arrows) with a short-axis diameter of 7 mm, a short-to-long-axis diameter ratio smaller than 0.5, and a visible hyperechoic hilum. **(b)** On corresponding US elastogram, the lymph node (arrows) is barely visible, has the same brightness as the surrounding muscle, and has very irregular and indistinct borders. The strain index for this lymph node is 0.7. **(c)** Power Doppler sonogram shows prominent hilar vascularization. Arrows point to the lymph node. Area inside square outline is the region of interest for power Doppler US. **(d)** Histologic sample shows incomplete metastatic involvement of papillary thyroid cancer (arrows). (Hematoxylin-eosin stain; original magnification, ×10.)

Post Hoc Power Analysis

The estimated proportions for the power analysis were based on the overall accuracies of the best B-mode US (short-to-long-axis diameter ratio > 0.5) and elastographic (strain index > 1.5) criteria for the diagnosis of metastatic lymph nodes (79% and 92%, respectively). According to the power analysis results, our sample had a power of 84% for detection of the difference between sonoelastography and routine B-mode US in the diagnosis of metastatic lymph nodes at a significance level of 5%. This finding supports the adequacy of the sample size used in our study.

Discussion

Diagnostic US is frequently used to assess cervical lymph nodes in patients with cancer. A variety of diagnostic criteria have been reported to be useful for the distinction between benign and metastatic lymph nodes. Lymph node size has been previously described as a criterion for malignancy detection, with

reported cutoff nodal short-axis diameters ranging from 5 to 30 mm (20,21). However, some findings indicate that the size criteria used for random patient populations are not optimal for neck lymph node assessment and that the same cutoff points cannot be used for all levels in the neck (22). In our study, a cutoff short-axis diameter of 8 mm was used, yet neither univariate nor multivariate analysis results support the diagnostic accuracy of this criterion for neck lymph node classification—mainly because of its low sensitivity.

Lymph node shape also has been used as a criterion for the detection of metastatic lymph nodes. In some previous studies, as well as in our current investigation, metastatic lymph nodes often appeared as round lesions, whereas benign nodes are usually flat or oval (23). The presence of a hyperechoic hilum and changes in the internal echogenicity of the nodes are usually considered strong diagnostic criteria for benign lymph nodes (24). It has been reported that 84%–92% of benign nodes but less than 5% of metastatic nodes have a hyperechoic hilum (25). On the other hand, some authors have reported that a hyperechoic hilum can be visualized in up to 51.5% of metastatic nodes (26). An absent lymph node hilum had high sensitivity but low specificity and overall accuracy. In contrast to this finding, abnormal lymph node echogenicity was a specific but not sensitive criterion.

Calcification in metastatic lymph nodes is generally rare (27,28). Some authors, however, have reported that about 68.7% of metastatic nodes from papillary cancer of the thyroid had calcification at US and histologic analysis (29). These findings are in disagreement with our results: Nodal calcifications were detected in only two of the lymph nodes that we examined, and they were specific but not sensitive.

Assessment of internal nodal vascularity at color or power Doppler US yielded additional criteria for the diagnosis of metastatic lymph nodes. It has been noted that benign lymph nodes tend to show hilar vascularity or appear avascular (30,31). In contrast, metastatic nodes tend to have peripheral or mixed (both peripheral and hilar) vascularity (32). In our study, power Doppler US vascularity had high specificity but low sensitivity. These findings correspond to previously published reports that the value of power Doppler US cannot compete with that of fine-needle aspiration biopsy in the diagnosis of metastatic adenopathy (33).

Our results in the differential diagnosis of metastatic lymph nodes at sonoelastography show that the majority of the benign nodes had the same brightness as the surrounding anatomic structures and therefore were not clearly visible on US elastograms. This is probably because of the small difference in elastic properties between benign lymph nodes and surrounding neck muscles. In contrast, the majority of the metastatic lymph nodes were partially or very visible and appeared substantially darker on the US elastograms. Again, these findings are probably related to the relative stiffness of metastatic lymph nodes compared with the elasticity of the surrounding muscles and other anatomic structures. However, additional studies of the real biomechanical properties of benign and metastatic lymph nodes performed by using previously elaborated measurement techniques are needed to elucidate these findings (34,35).

The margins of the metastatic lymph nodes on US elastograms were more regular and distinct than the margins of the benign lymph nodes. This finding might reflect the greater difference in elastic properties between metastatic lymph nodes and surrounding tissues or a certain desmoplastic reaction that creates a stiff rim around metastatic lymph nodes. All of the visual elastographic

Figure 5

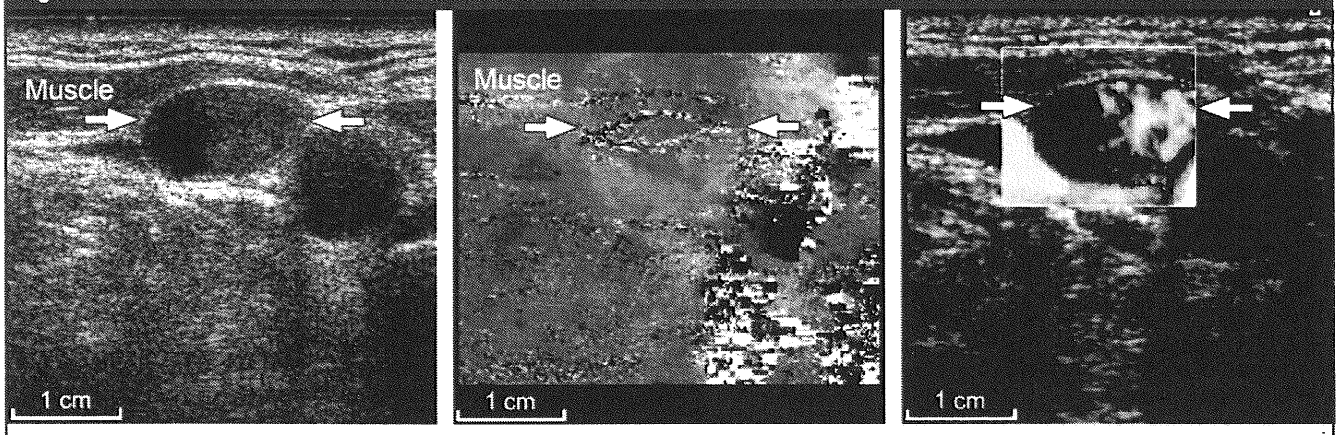

a. b. c.

Figure 5: Metastatic lymph node with central necrosis. **(a)** Gray-scale sonogram obtained in 57-year-old man with papillary thyroid cancer shows metastatic lymph node (arrows) with a short-axis diameter of 9 mm, a short-to-long-axis diameter ratio smaller than 0.5, an absent hyperechoic hilum, and mixed echogenicity. **(b)** On corresponding US elastogram, the lymph node (arrows) is barely visible, has the same brightness as the surrounding muscle, and has very irregular and indistinct borders. **(c)** Power Doppler sonogram shows prominent peripheral vascularization. Arrows point to the lymph node. Area inside square outline is the region of interest for power Doppler US.

criteria examined in our study, although promising, had low diagnostic accuracy and were comparable in accuracy to the routine US criteria.

On the other hand, quantitative elastographic measurements of relative lymph node elasticity, obtained by comparing the absolute values of lymph node strain with the absolute values of surrounding muscle strain, had the best diagnostic accuracy of all the US and elastographic criteria evaluated. Our results show that the majority of benign lymph nodes were less than 1.5 times stiffer than the surrounding muscles and that the majority of the metastatic lymph nodes were more than 1.5 times stiffer. The high diagnostic accuracy of this criterion was confirmed by the results of multivariate regression analysis. This finding suggests that sonoelastography can be helpful in the selection of suspicious neck lymph nodes that should be examined at percutaneous biopsy and/or nodal dissection for accurate preoperative staging and individual therapy selection for patients with thyroid or hypopharyngeal cancer.

Some of the limitations of our study should be addressed. During histologic examination, only two or three tissue slices per lymph node were examined; therefore, we could not accurately assess the extent of tumor involvement in the nodes. This should be investigated in detail in the future, because the severity of metastatic involvement may affect the strain characteristics of a lymph node. In addition, the difference in elastic properties between the benign and metastatic lymph nodes measured at sonoelastography was not confirmed by direct measurements of the biomechanical properties of the examined tissues removed at surgery. Thus, future studies that yield the biomechanical data needed to support correct interpretations of abnormal US elastograms are warranted. Because of the study design, we were unable to assess the observers' ability to diagnose thyroid cancer on the basis of the elastogram findings. Therefore, future studies to evaluate the inter- and intraobserver variability and the reliability of sonoelastography in the detection of metastatic lymph node involvement are needed.

At present, the methods used to perform sonoelastography are not ideal. Real-time elastography, which is incorporated into some commercially available US scanners, involves the use of fast strain image reconstruction algorithms. However, this technique is not as accurate as the off-line processing of strain images. On the other hand, off-line processing of US elastograms, as performed in the present study, is too time consuming and labor intensive to be used in busy clinical settings. Thus, future advances in image acquisition and reconstruction algorithms are needed to improve image quality and increase the clinical utility of this method. In addition, the image quality and diagnostic performance of US elastograms acquired with freehand compression depend substantially on the quality of the compression and the specifications of the elasticity formation algorithms.

In the present study, the overall quality of the strain images was substantially affected by decorrelation noise, which resulted from the nonaxial and out-of-plane motion of the examined lesions and from the pulsation of the carotid artery. This problem may be partially solved when the computational capability of US systems increases to the extent that we can acquire higher quality primary images at high frame rates. Another drawback is that the compression load applied with freehand elastography is not standardized and thus may result in some inter- and intraobserver variability. All of these issues require thoughtful elaboration in the future to improve the diagnostic accuracy of sonoelastography in patients with cancer.

In conclusion, sonoelastography is a promising imaging technique that can provide assistance in the differentiation of benign and metastatic neck lymph nodes. Our findings suggest that sonoelastography can be helpful in the selection of suspicious neck lymph nodes that should be examined at cytologic examination or open biopsy for accurate preoperative staging and individual therapy selection for patients suspected of having thyroid or hypopharyngeal cancer.

Acknowledgments: We sincerely thank Siemens Medical Systems, Ultrasound Group, Issaquah, Wash, for technical assistance. We gratefully acknowledge the efforts of Junji Konishi, MD, PhD, Emeritus Professor, Department of Nuclear Medicine and Diagnostic Imaging, Kyoto University Graduate School of Medicine, for his insightful advice and support during the preparation of this study. In addition, the authors thank Hirokazu Kotani, MD, PhD, from the Laboratory of Anatomic Pathology, Kyoto University Hospital, for his help with histologic examination. The authors also sincerely thank Yu Shyr, PhD, from Vanderbilt-Ingram Cancer Center, Vanderbilt University School of Medicine, for his valuable help with the statistical analyses.

References

1. Senchenkov A, Staren ED. Ultrasound in head and neck surgery: thyroid, parathyroid, and cervical lymph nodes. Surg Clin North Am 2004;84:973–1000.
2. Lyshchik A, Drozd V, Demidchik Y, Reiners C. Diagnosis of thyroid cancer in children: value of gray-scale and power Doppler US. Radiology 2005;235:604–613.
3. Kau RJ, Alexiou C, Stimmer H, Arnold W. Diagnostic procedures for detection of lymph node metastases in cancer of the larynx. ORL J Otorhinolaryngol Relat Spec 2000;62:199–203.
4. Ahuja A, Ying M, Evans R, King W, Metreweli C. The application of ultrasound criteria for malignancy in differentiating tuberculous cervical adenitis from metastatic nasopharyngeal carcinoma. Clin Radiol 1995; 50:391–395.
5. Gritzmann N, Hollerweger A, Macheiner P, Rettenbacher T. Sonography of soft tissue masses of the neck. J Clin Ultrasound 2002; 30:356–373.
6. Ophir J, Cespedes I, Ponnekanti H, Yazdi Y, Li X. Elastography: a quantitative method for imaging the elasticity of biological tissues. Ultrason Imaging 1991;13:111–134.
7. Ophir J, Alam SK, Garra B, et al. Elastography: ultrasonic estimation and imaging of the elastic properties of tissues. Proc Inst Mech Eng [H] 1999;213:203–233.
8. Chaturvedi P, Insana MF, Hall TJ. Testing the limitations of 2-D companding for strain imaging using phantoms. IEEE Trans Ultrason Ferroelectr Freq Control 1998;45:1022–1031.
9. Garra BS, Cespedes EI, Ophir J, et al. Elas-

tography of breast lesions: initial clinical results. Radiology 1997;202:79–86.

10. Lyshchik A, Higashi T, Asato R, et al. Thyroid gland tumor diagnosis at US elastography. Radiology 2005;237:202–211.
11. Cochlin DL, Ganatra RH, Griffiths DF. Elastography in the detection of prostatic cancer. Clin Radiol 2002;57:1014–1020.
12. Solbiati L, Cioffi V, Ballarati E. Ultrasonography of the neck. Radiol Clin North Am 1992; 30:941–954.
13. Ahuja A, Ying M. An overview of neck node sonography. Invest Radiol 2002;37:333–342.
14. Steinkamp HJ, Wissgott C, Rademaker J, Felix R. Current status of power Doppler and color Doppler sonography in the differential diagnosis of lymph node lesions. Eur Radiol 2002;12:1785–1793.
15. Chaturvedi P, Insana MF, Hall TJ. 2-D companding for noise reduction in strain imaging. IEEE Trans Ultrason Ferroelectr Freq Control 1998;45:179–191.
16. Pellot-Barakat C, Mai JJ, Kargel C, Herment A, Trummer B, Insana MF. Accelerating ultrasonic strain reconstructions by introducing mechanical constraints. In: Sonka M, Fitzpatrick MJ, eds. Proceedings of SPIE: medical imaging 2002. Vol 4684. Bellingham, Wash: International Society for Optical Engineering, 2002; 323–333.
17. Liang KY, Zeger SL. Longitudinal data analysis using generalized linear models. Biometrika 1986;73:13–22.
18. Diggle P, Liang KY, Zeger SL. Analysis of longitudinal data. Oxford, England: Clarendon, 1994.
19. Rosner B. Fundamentals of biostatistics. 4th ed. Belmont, Calif: Wadsworth, 1995.
20. Ying M, Ahuja A, Metreweli C. Diagnostic accuracy of sonographic criteria for evaluation of cervical lymphadenopathy. J Ultrasound Med 1998;17:437–445.
21. Hajek PC, Salomonowitz E, Turk R, Tscholakoff D, Kumpan W, Czembirek H. Lymph nodes of the neck: evaluation with US. Radiology 1986;158:739–742.
22. van den Brekel MW, Castelijns JA, Snow GB. The size of lymph nodes in the neck on sonograms as a radiologic criterion for metastasis: how reliable is it? AJNR Am J Neuroradiol 1998;19:695–700.
23. Papakonstantinou O, Bakantaki A, Paspalaki P, Charoulakis N, Gourtsoyiannis N. High-resolution and color Doppler ultrasonography of cervical lymphadenopathy in children. Acta Radiol 2001;42:470–476.
24. Ying M, Ahuja AT, Evans R, King W, Metreweli C. Cervical lymphadenopathy: sonographic differentiation between tuberculous nodes and nodal metastases from non-head and neck carcinomas. J Clin Ultrasound 1998;26:383–389.
25. Rubaltelli L, Proto E, Salmaso R, Bortoletto P, Candiani F, Cagol P. Sonography of abnormal lymph nodes in vitro: correlation of sonographic and histologic findings. AJR Am J Roentgenol 1990;155:1241–1244.
26. Vassallo P, Wernecke K, Roos N, Peters PE. Differentiation of benign from malignant superficial lymphadenopathy: the role of high-resolution US. Radiology 1992;183:215–220.
27. Weber AL, Randolph G, Aksoy FG. The thyroid and parathyroid glands: CT and MR imaging and correlation with pathology and clinical findings. Radiol Clin North Am 2000; 38:1105–1129.
28. Bruneton JN, Normand F. Cervical lymph nodes. In: Bruneton JN, ed. Ultrasonography of the neck. Berlin, Germany: Springer-Verlag, 1987; 81–92.
29. Ahuja AT, Chow L, Chick W, King W, Metreweli C. Metastatic cervical nodes in papillary carcinoma of the thyroid: ultrasound and histological correlation. Clin Radiol 1995; 50:229–231.
30. Dragoni F, Cartoni C, Pescarmona E, et al. The role of high resolution pulsed and color Doppler ultrasound in the differential diagnosis of benign and malignant lymphadenopathy: results of multivariate analysis. Cancer 1999;85:2485–2490.
31. Stramare R, Tregnaghi A, Fitta C, et al. High-sensitivity power Doppler imaging of normal superficial lymph nodes. J Clin Ultrasound 2004;32:273–276.
32. Sakaguchi T, Yamashita Y, Katahira K, et al. Differential diagnosis of small round cervical lymph nodes: comparison of power Doppler US with contrast-enhanced CT and pathologic results. Radiat Med 2001;19:119–125.
33. Giovagnorio F, Caiazzo R, Avitto A. Evaluation of vascular patterns of cervical lymph nodes with power Doppler sonography. J Clin Ultrasound 1997;25:71–76.
34. Krouskop TA, Wheeler TM, Kallel F, Garra BS, Hall T. Elastic moduli of breast and prostate tissues under compression. Ultrason Imaging 1998;20:260–274.
35. Lyshchik A, Higashi T, Asato R, et al. Elastic moduli of thyroid tissues under compression. Ultrason Imaging 2005;27:101–110.

研　究　論　文

Dosimetric properties of the liquid ionization chamber electronic portal imaging device (EPID)

Kunihiko Tateoka[1),2)*], Atsushi Ouchi[3)], Masaaki Waka[4)], Kensei Nakata[3)], Daiki Nagase[2)], Kazunari Shimizume[2)], Tsunehiko Saikawa[2)], Masato Hareyama[1),2),3)]

[1)] *Radiation Oncology, Imaging and Diagnosis, Molecular and Organ Regulation, Sapporo Medical University, Graduate School of Medicine*

[2)] *Division of Radiology and Nuclear Medicine, Sapporo Medical University Hospital, School of Medicine*

[3)] *Department of Radiology, Sapporo Medical University, School of Medicine*

[4)] *Department of Radioisotope Research, Sapporo Medical University, School of Medicine Biomedical Research, Education and Instrumentation Center*

Research Code No.: 203.9

Key words: EPID, Photon Dosimetry

Abstract

In the relation between the pixel values of the electronic portal imaging device (EPID) and dose rate, pixel values have been reported to be proportional to the square roots of the dose rates although some researchers have reported that each EPID pixel value was almost proportional to the dose rates when they were more than 1 Gy/min. To resolve this contradiction, in this study we have investigated the dosimetric properties of the liquid ionization chamber EPID based on a two-dimensional matrix of liquid-filled ionization chambers. Our results show that the pixel values of this EPID were proportional to the square roots of the dose rates when they were less than 0.5 Gy/min, and the values were proportional to the dose rates when they were more than that. In addition, the survival time of electrons in the liquid of the EPID is reportedly dependent on the amount of impurities in the liquid ionizing chamber of EPID. The pixel values of the EPID acquired in rapid succession, increased. In the results, the pixel values were constantly increased to approximately 0.2% of pre-images for less than 15 s of the rest interval. When changes in the sensitivity of each pixel value were

* 札幌医科大学付属病院放射線部〔〒060-8543 札幌市中央区南1条西16丁目291〕: Radiation Oncology, Imaging and Diagnosis, Molecular and Organ Regulation, Sapporo
E-mail: tateoka@sapmed.ac.jp

approximately 1%, approximately 5% changes were observed against the transformed dose rate. To avoid this difference, we developed the following formula relating the pixel value, P, and dose rate, D.

$$P = a \cdot D + b - k \cdot h$$

(a, b, h: constants, k: variable)

Received Dec.21, 2005; revision accepted Feb.10, 2006

I. Introduction

Radiotherapy has been verified by image verification, in which portal images are compared visually with simulation images or digitally reconstructed radiographs (DRRs). Image verification has been developed which uses electronic portal imaging devices (EPIDs) that are computer-controlled through an on-line connection with an actuator. Generally, there are three types of EPIDs: a mirror-based video system, a fiber-optic video system, and a liquid ionization chamber system[1]. Although the image collecting methods are different, image verification can be conducted in a short time without interrupting the process of film development to obtain an EPID image on-line[2]. Moreover, dose verification is an essential process in radiotherapy.

Thus far, dose verification has been performed using a thermoluminescent dosimeter (TLD) placed in an anthropomorphic phantom and by measuring the dose that penetrates into the body, by film. However, measurements using TLDs and semiconductor detectors can be done at only a few points simultaneously, and the film method is not satisfactory with respect to clinical applications because of the film development time[3-7].

Recently, studies have been conducted to verify the possibility of using EPID images as a dosimeter to verify the penetrated dose[8-16]. Van Herk[10] indicated that using the liquid ionization chamber EPID, the square roots of dose rates and the EPID signal pixel values were proportional. On the basis of his study, many researchers obtained corrected dose rates from the measured EPID pixel values. However, Essers et al.[8] reported that in the measurement system for an aerial dose rate using a small phantom, dose rates and EPID signals were proportional when dose rates were more than 1 Gy/min. Curtin-Savard and Podgorsak[16] attributed the observation of Essers et al. to the amount of electric charge being constantly increased by contaminants in the isooctane used as an ionization layer of the EPID in the sequential image collection over a short time. Zhu et al.[14] reported that the EPID showed a maximum change of 3% in the sensitivity during 90-day period, and showed a standard deviation within 1.2% as daily changes. Essers et al.[8] suggested that the influence of scattered material included within the EPID could not be ignored. On the other hand, Zhu et al.[14] considered that there is no major effect from scattered material based on the fact that EPID signals were obtained on irradiation fields of various sizes.

However, the relative differences in the amounts of electric charges between EPID dosimetry and conventional dosimetry with a farmer type cylindrical ionization chamber and a solid phantom have

not been distinguished.

The purpose of this paper is to elucidate dosimetric properties of the ionization chamber EPID system. We have quantified the fluctuation of the pixel values depending on the image collection conditions and the change in the amount of electric charges due to impurity in the liquid ionization chamber.

II. Materials and Methods

A. Equipment

The liquid ionization chamber EPID (Portal Vision System, Varian Medical System, Palo Alto, CA) used in this study was installed with the linear accelerator (CLINAC2100C, Varian Medical System, Palo Alto, CA) that generated 4 MV and 10 MV. The ionization chamber was sequenced in the matrix of 256 × 256 pixels (total 65536 pixels). The image collection area was 32.5 cm × 32.5 cm. There were two pole boards (printed circuit boards, PCBs) on the upper and lower sides of the ionization layer which was a 1 mm thick isooctane phase. A 1 mm thick layer of barium and plastic material (density: 4.75 g/cm^3) on the upper surface of the PCB functioned as the build-up material of the X-rays. Each pixel was 1.27 mm × 1.27 mm × 1.0 mm. The front and back of the build-up region were approximately 10 mm and 5 mm of water equivalent material, respectively[8-13].

The dosimetric properties were evaluated from the dose determined by using EPID (L-EPID dose) and the values from the farmer type cylindrical ionization chamber (NE2581, NE Technology Ltd., Berkshire, UK). The area of the irradiation field was decided as 10 cm × 10 cm, and source-to-surface distance (SDD) was 100 cm. Tough Water (Kyoto Kagaku Co., Ltd., Kyoto, Japan) was used as a solid phantom for the measurement. The depth for the measurement point at 4 MV and 10 MV was fixed at the depth of dose maximum (dmax) (4 MV: 1.0 cm and 10 MV: 2.5 cm). For the measurement using the farmer type cylindrical ionization chamber, the thickness of Tough Water below the measurement point was prepared as 5 mm to replicate the geometrical arrangement of the image from the EPID.

To confirm build-up area in front of the EPID surface, tissue maximum ratio (TMR) was measured at 4 MV and 10 MV. The EPID pixel values were a maximum value at X-ray energies of 4 MV and 10 MV when Tough Water thickness was adjusted to 3 mm and 18 mm, respectively, and these Tough Water thicknesses were used for the study. To avoid variations in the pixel values, the mean value of 11 × 11 pixels was used as the EPID pixel value on the central axis of the X-ray beam. Variation in the mean values was within approximately 0.5% of the standard deviation. Moreover, to

Table I　EPID conditions for 4 MV X-rays with 250 MU/min and 10 MV X-rays with 240 MU/min .

Energy	4MV	10MV
MU/min	250	240
Sync Frequency	400Hz	180Hz
Interpulse Distance	2.50ms	5.56ms
HV Row Cycle Time	12.50ms	11.11ms
number of Pulses Used for on Sync	5pulses	2pulses
number of row per sync pulse	1row	1row
number of Averages (Row Sweeps)	2scans	1scans
Total Acquision time	3.35sec	2.98sec

minimize the influence of the variation, we used the average of 10 images which decreased the standard deviations of the changes to 0.2%. The settings of the EPID and the accelerator are shown in Table I. Ionex Dose Master 2590B (NE Technology Ltd., Berkshire, UK) was used as the electrometer.

B. Measurement of dosimetric properties

1. Effect of contaminants on the liquid ionization chamber EPID

Isooctane in the ionization layer of the liquid ionization chamber is known to contain some contaminants. These contaminants may affect the survival time of the electric charge because they delay movement of the electric charge in isooctane[8]. On observing the phenomena, we concluded that the pixel values increase with continued collection during the survival time of the electric charge. To examine the effects of contaminants in isooctane on the pixel values, we measured four series of ten EPID images (groups A, B, C, and D). Each measurement group was comprised of 10 images and their image acquisition interval (rest interval) was 5, 15, 30, and 60 s, respectively. The collection interval between each measured group was 120 s.

2. The dosimetric properties of EPID as reported by Van Herk

As the voltage is supplied to the ionization chamber in L-EPID with the ray pulse of the accelerator, the voltage supply time is shorter than the movement time to the pole of an ion pair generated by the X-ray beam and its survival time. On the other hand, in the measurement used for a conventional ionization chamber, the voltage supply time is longer than the movement time to the pole of an ion and its survival time, because voltage is continuously supplied during the period in which a ray is irradiated as a pulse. It is considered, on the basis of these facts, that the collecting method of ions using EPID is different from that using the conventional ionization chamber.

Van Herk[10] proposed a new theory concerning the collecting method of ions using L-EPID. According to this theory, in each ionization chamber, ion pairs, $n(t)$ are generated by an X-ray beam, and the changing rate, $dn(t)$/dt, against the time $n(t)$ contains two changing rates of positive and negative ions. The total numbers of ion pairs, $N_{in}(t)$ is proportional to the dose rate, D, and to the number of positive ions, $n(t)+$ and negative ions, $n(t)-$,because in this case, negative ions imply ion recombination.

On the basis of the consideration mentioned above, the number of ion pairs, $dn(t)/dt$ is given by the following formula,

$$\frac{dn(t)}{dt} = N_{in}(t) - an(t)^2 \qquad (1)$$

where α is a constant.

However, as with long time irradiation, the generation of new ion pairs balances the loss of ion pairs caused by the ion recombination, the left side of formula (1) becomes zero ($dn(t)/dt = 0$) and

$n(t)$ is expected to be $n(t) \equiv n_{eq}$. Therefore, n_{eq} is expressed by formula (2).

$$n_{eq} = \sqrt{\frac{N_{in}}{a}}$$
$$n_{eq} = \sqrt{\frac{\beta}{a} \cdot D} \qquad (2)$$

Here, $N_{in} = \beta \times D$ and β is a constant. According to this formula, the EPID pixel values are proportional to the square root of dose rate. To confirm the above formula and to examine the relationship between the actual dose and the EPID pixel value, we collected EPID images using 4 MV and 10 MV X-rays while changing the dose rate and while changing the thickness of the lead board on the tray of the accelerator from 0 mm to 80 mm. In addition, under the same conditions, the dose rate was measured with a farmer type cylindrical ionization chamber. On the basis of these results, a characteristic curve for the EPID was obtained.

3. Effect of scattered radiation

An arbitrary ionizing chamber is affected by scatter radiation generated from surrounding EPID ionizing chambers. To evaluate the effect, L-EPID images were collected while changing radiation field sizes from 4 cm × 4 cm to 20 cm × 20 cm. Each image was converted to a dose rate using the characteristic curve and then the dose rates were compared with those measured under identical conditions by the farmer type cylindrical ionization chamber.

III. Results

A. Effects of contaminants in the liquid ionization chamber

In the case where image-collecting intervals were below 15 s (measurement Groups A and B), the pixel values increased slightly (approximately 0.06%) in each EPID image. As compared with the initial image, the pixel value of the 10th image increased from approximately 1.0% to 1.3%. When the image-collecting intervals were set at more than 30 s (Groups C and D), the change in the pixel value was within approximately ±0.25% and was stable. These results agreed with those described by Curtin-Savard and Podgorsak[15].

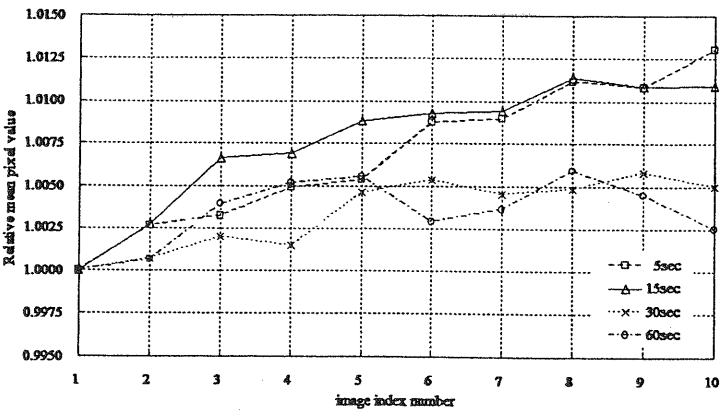

Fig. 1 Reproducibility of mean pixel value for four series of ten EPID images obtained under the same conditions at a 250 MU/min, 100 cm SOD, and 10 cm × 10 cm field size on the central axis at the maximum depth with 4 MV X-rays. The rest intervals between image acquisitions were 5, 15, 30, and 60 s. The region of interest for calculating the mean consisted of 11 × 11 pixels centered on the central field. The mean pixel values were normalized to 1.0 for the first image of each series.

Moreover, the difference in pixel values between the first image of Group B and that of Group D was approximately 1.6%. On the basis of these results, we decided to use a 30 s interval of image collection (Group C) using the EPID (Fig.1).

B. The dosimetric properties of the EPID

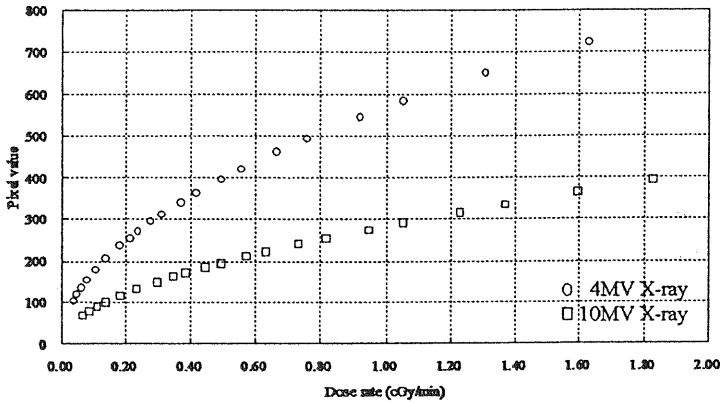

Fig. 2 Plot of the relation between the pixel value and the dose rate. Dose rate was determined with the farmer type cylindrical ionization chamber on the central axis at the maximum depth for a 10 cm×10 cm field size and 100 cm SOD with 4 MV (circle) and 10 MV X-rays (square). Pixel values were averaged over 11×11 pixels around the center of the field.

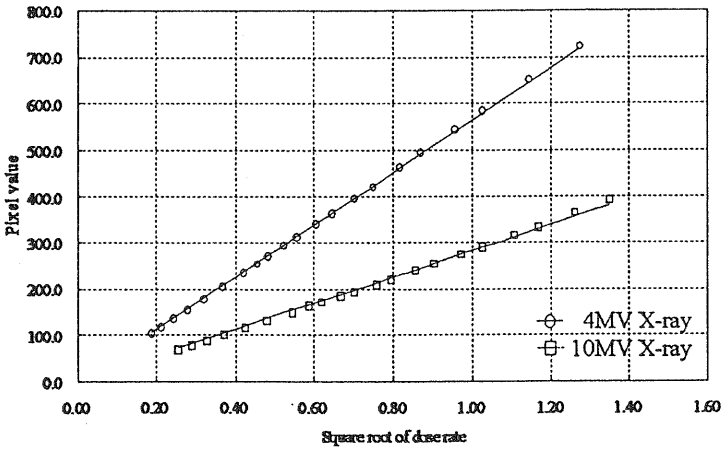

Fig. 3 Plot of the relation between pixel values and the square root of the dose rate. Dose rate was determined with the farmer type cylindrical ionization chamber on the central axis at the maximum depth for a 10 cm×10 cm field size and 100 cm SOD with 4 MV (circle) and 10 MV X-rays (square). The solid line represents an approximate value according to Van Herk's theory 10). Pixel values were averaged over 11×11 pixels around the center of the field.

In Fig. 2, pixel value is plotted against the dose rate for each thickness value of the lead board measured with the farmer type cylindrical ionization chamber. The pixel values increased rapidly at a low dose rate, at 4 MV or 10 MV. When the dose rate exceeded 0.5 Gy/min, the pixel values showed a gradual increase.

The pixel values shown in Fig. 2 were calculated on the basis of Van Herk's theory[10] and these calculated values are shown in Fig. 3. The relationship between the pixel values and the square roots of the dose rates was linear, but not a strict one. To elaborate, in the range in which the pixel values increased rapidly against the dose rates, the pixel values showed an approximately proportional increase with the square roots of the dose rates. In the range in which the pixel values showed a gradual increase, the pixel values showed an approximate proportional increase to the dose rates themselves.

The results presented in this study were in good agreement with those reported by Essers et al.[8]. The relationship between pixel values and dose rates regressed as the secondary formula to the square root of the dose rates. Approximate formulas at 4 MV and 10 MV are shown in Eqs. (3) and (4), respectively.

$$P=3.2381D+569.08\sqrt{D}-5.5168 \qquad R^2=1.0000 \tag{3}$$

$$P=22.085D+260.32\sqrt{D}+0.1266 \qquad R^2=1.0000 \tag{4}$$

P: pixel value, D: dose rate (cGy/min), :R^2 coefficient of determination.

From these results, the abovementioned formulas were considered to be a good tool for calculation of EPID doses from the measured pixel values.

C. Effects of scattered radiation

Fig. 4 shows the EPID doses with respect to the changes in the size of the irradiation field. EPID doses showed a marked increase till the area of the irradiation field was increased to 12 cm × 12 cm, while the increase was gradual when the area of the irradiation field was increased above that. Fig. 5 indicates the total scatter correction factor (Sc,p) obtained from data of the EPID and the farmer type cylindrical ionization chamber at 4 MV. There was a tendency for the Sc,p value of EPID dose to increase with field size in comparison with that from the farmer type cylindrical ionization chamber. Sc,p values from the EPID were higher by 1.2% than those from the farmer type cylindrical ionization chamber for a 20 cm × 20 cm area irradiation field and were higher by less than 1% for a 15 cm × 15 cm area irradiation field. On the other hand, for the irradiation of 10 MV, the opposite phenomena was observed, i.e., Sc,p values from the EPID decreased. The values from the EPID were 0.8% lower and less than 0.2% of those from the farmer-type cylindrical ionization chamber for a 4 cm × 4 cm area irradiation field and other field sizes, respectively.

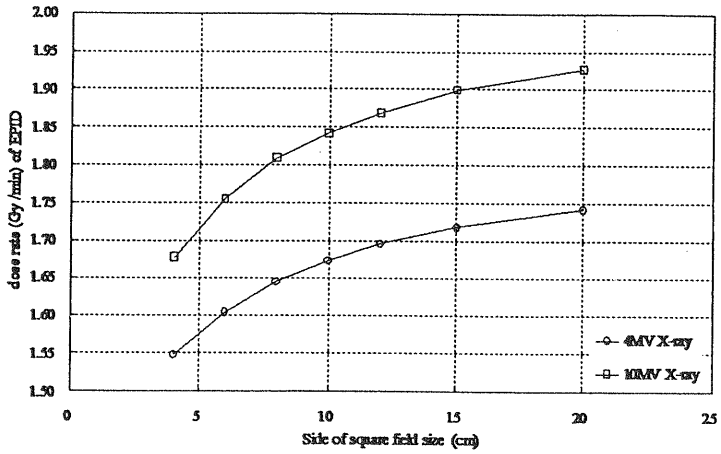

Fig. 4 EPID dose rates obtained from pixel values of the field sizes from 4 cm × 4 cm to 20 cm × 20 cm. The measurements were done at the maximum depth on the central axis for a 100 cm SOD with 4 MV and 10 MV X-rays. Pixel values were averaged over 11 × 11 pixels around the center of the field.

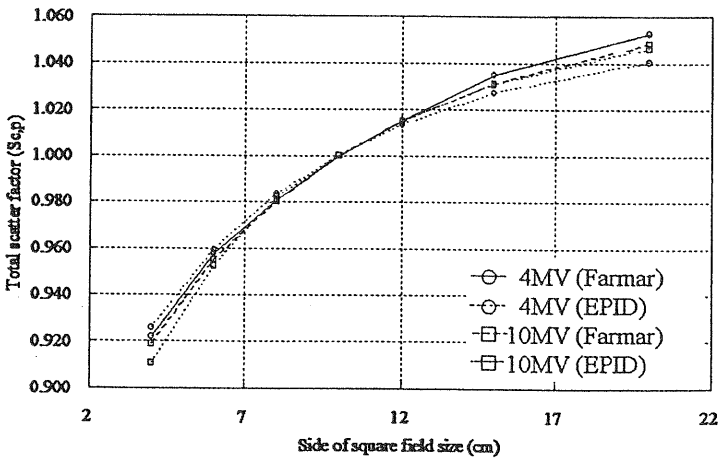

Fig. 5 The total scatter factor (Sc,p) of the dose rates obtained from pixel values of the EPID and the farmer type cylindrical ionization chamber. The measurements were done at the maximum depth on the central axis for a 100 cm SOD with 4 MV and 10 MV X-rays. The dose rates were normalized to 1.0 for 10 cm × 10 cm field sizes. Pixel values were averaged over 11 × 11 pixels around the center of the field.

Ⅳ. Discussion

It was considered, based on the results, that when the collection interval was short, the pixel values increased, and when it was long, few increments in pixel value occurred. Therefore, an interval of over 30 s was considered to be a good condition for image collection. With respect to the ionizing phenomenon, it was suggested that electric charges in the liquid ionizing chamber of L-EPID were almost saturated at a collection interval of more than 30 s, but some electric charges remained when the collection interval was shorter.

It was speculated that the causes of pixel value deviations between the first image and other images included in each collection Group are the changes in temperature within ionizing chambers according to the voltage supply to the L-EPID.

Stable pixel values independent of the cumulative irradiation dose are required for precise dosimetric verification, since small differences of pixel value as mentioned above lead to large ones in the converted EPID dose. L-EPID images should be collected under a suitable condition wherein few pixel values are affected by residual electric charge.

As described by Van Herk[10], the relationship between pixel values and dose rates indicated that the pixel values were approximately proportional to the square root of the dose rates. However, we observed that pixel values increased gradually, when X-ray dose exceeded 0.5 Gy/min (Fig. 2). In the case of irradiation less than 0.5 Gy/min using 4 MV or 10 MV X-rays, the pixel values had an approximately proportional increase to the square root of the dose rates. For an irradiation of more than 0.5 Gy/min, pixel values showed an approximate proportional increase with the dose rates. This result led us to consider that the theory described by Van Herk[10] required modification. We propose a new improved formula for Eq. (1) in our hypothesis, as follows.

In sequential acquisition of L-EPID images, it was assumed that there were three phenomena: (1) the generation of new ion pairs balances the loss of ion pairs caused by the ion recombination; (2) the generation of new ion pairs exceeds loss of ion pairs caused by the ion recombination; and (3) fluctuation of sensitivity of the liquid ionizing chamber occurs with setup conditions for image collection.

In an irradiation process over a substantial length of time, the added concentration of ion pairs by generation and recombination should be considered. Moreover, a correction term for sensitivity, C, is required. Therefore, the measured final concentration of ion pairs, N_{final} is expressed as follows.

$$N_{final} = n_{eq} + \frac{dn(t)}{dt} + c$$
$$= \sqrt{\frac{N_{in}}{a}} + \{N_{in}(t) - an(t)^2 + C\} \quad (5)$$

Where C is constant. For N_{in} to be equal to $\beta \cdot D$, Eq. (5) can be converted to the following secondary formula with respect to the square root of the dose rates.

$$N_{final}=\beta \cdot D+\sqrt{\frac{\beta}{a}\cdot D-an(t)^2+C} \qquad (6)$$

Then, as the relation between pixel value, (P) and concentration of ion pairs is $P=\gamma \cdot N_{final}$, Eq. (6) can be changed to Eq. (7).

$$P=a\cdot D+b\cdot\sqrt{D}-h \qquad (7)$$

Here, a and b are constants, h is the constant for loss of ion pairs caused by ion recombination and for the sensitivity correction factor of ionizing chambers. Hence, $h=\gamma(\cdot a\cdot n(t)^2+C)$. The relationship between the pixel values and the dose rates in Eq. (7) can be given as a secondary dimension quantic formula the same as the approximate Eq. (3), (4) as above mentioned.

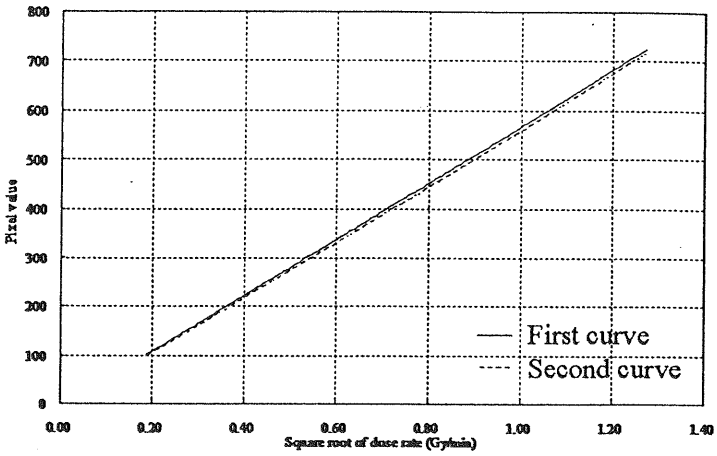

Fig. 6 Plot of the relation between the pixel values and the square roots of the dose rates determined using the farmer type cylindrical ionization chamber on the central axis at maximum depth for field size (10 cm × 10 cm) and SOD (100 cm) with 4 MV X-rays. The second curve was determined 14 days after the first curve. Pixel values were averaged over 11 × 11 pixels around the center of the field.

The characteristic curve of the pixel values from the EPID at 4 MV were rearranged (Fig. 6) for assessment of the sensitivity correction factor (h). The obtained curve indicated that sensitivities of the pixels decreased. The pixel values decreased 1.1% similar to the daily changes mentioned above. However, EPID doses showed 5.5% and 3.8% decreases in high dose and low dose regions, respectively. The values in this study were in good agreement with those reported by Zhu et al.[14].

When we multiplied h by 2.47, the difference in the EPID dose rate was within ± 0.1%. We, now, introduce a constant (k) as a correction factor for the daily deviation of the sensitivity of the ionizing chamber.

According to the consideration, formula (7) was changed as follows.

$$P=a\cdot D+b\cdot\sqrt{D}-k\cdot h \qquad (8)$$

Eq. (8) implies that the characteristic curve of the pixel values does not need to be constructed, we have to acquire k as a factor for the daily deviation from measurements in the standard irradiation field.

The effect of the scattered rays on sensitivity in the EPID was speculated to depend on the effects of the water equivalent materials and PCB in the front, back, and supports of the EPID structure. For 4 MV, the effects of the scattering body in the back were stronger than those for 10 MV,

and the difference of Sc,p values between the L-EPID and farmer type cylindrical ionization chamber was considered to be high.

V. Conclusions

We quantified effects from contaminants and the sensitivity variation in the electric charge layer with the liquid ionization chamber EPID from the viewpoint of image collection setting. Further, we revised the theory presented by Van Herk [10] for the dose rate of L-EPID, which led to the following equation.

$$P = a \cdot D + b \cdot \sqrt{D} - k \cdot h \tag{8}$$

h: changes in effect from the contaminant concentration in electric charge layer, k: sensitivity correction factor of daily deviation.

By using this formula, the obtained pixel values were converted into the dose rates within $\pm 0.1\,\%$ errors.

Acknowledgments

We thank Professor Masao Hoshina, Department of Radiology, Gunma Prefecture College of Health Science, and Dr. Jack Yang, Institute for Advanced Radiation Oncology, Monmouth Medical Center for useful discussions and advice.

References

1) Boyer AL, Antonuk L, Fenster A et al.: A review of electronic portal imaging devices (EPIDs). Med. Phys. 19: 1–16, 1992
2) Meertens, Van Herk M, Bijhold J and Bartelink H: First clinical experience with a newly developed electronic portal imaging device. Int. J. Radiat. Oncol. Biol. Phys. 18: 1173–1182, 1990
3) Gilhuijs KAG, Touw A, Van Herk M and Vijlbrief RE: Optimization of automatic portal image analysis. Med. Phys. 22: 1089–1099, 1995
4) Ruden BI: Evaluation of the clinical use of TLD. Acta. Radiol. Ther. Phys. Biol. 15: 447–464, 1976
5) Eunens G, Van Dam J, Dutreix A and Van der Schueren E: Quality assurance in radiotherapy in vivo dosimetry. 1. Entrance dose measurement, a reliable procedure. Radiother. Oncol. 22: 285–289, 1991
6) An Dam J, Vaerman C, Blancket N et al.: Are port films reliable for in vivo exit dose measurement?. Radiother. Oncol. 25: 67–72, 1992
7) Fiorino C, Del Vacchio A, Cattaneo GM et al.: Exit dose measurement by portal film dosimetry. Radiother. Oncol. 29: 336–340, 1993
8) Essers M, Hoogervorst BR, Van Herk M, et al.: Dosimetric characteristics of a liquid filled elec-

tronic portal imaging device. Int. J. Radiat. Oncol. Biol. Phys. 33: 1265－1272 , 1995
9) Yin FF, Schell MC and Rubin P: Input/output characteristics of a matrix ion-chamber electronic portal imaging device. Med. Phys. 2: 1447－1454, 1994
10) Van Herk M: Physical aspects of a liquid－filled ionization chamber with pulsed polarizing voltage. Med. Phys. 18: 692－702. 1991
11) Kirby MC and Williams PC: Measurement possibilities using an electronic portal imaging device. Radiother. Oncol. 29: 237－243, 1993
12) Heijment BJM, Pasma KL, Kroonwijk M, et al.: Portal dose measurement in radiotherapy using an electronic portal imaging device (EPID). Phys. Med. Biol. 40: 1943－1955, 1995
13) Essers M, Boellaard R, Van Herk M, et al.: Transmission dosimetry with a liquid filled electronic portal imaging device: Int. J. Radiat. Oncol. Biol. Phys. 34: 931－941, 1996
14) Zhu YZ, Jiang XQ and Van Dyk J: Portal dosimetry using a liquid ion chamber-dose response studies. Med. Phys. 22: 1101－1106, 1995
15) Curtin-Savard AJ and Podgorsak EB: An electronic portal imaging device as a physics tool. Med. Dosimetry 22: 101－105, 1997
16) Curtin-Savard AJ and Podgorsak EB: Verification of segmented beam delivery using a commercial electronic portal imaging device. Med. Phys. 26: 737－742, 1999

Radiotherapy and Oncology 79 (2006) 179-184
www.thegreenjournal.com

Lymphoma

Analyses of dose-response in radiotherapy for patients with mature T/NK-cell lymphomas according to the WHO classification

Koh-ichi Sakata[a,*], Nobukazu Fuwa[b], Takeshi Kodaira[b], Kazunori Aratani[c], Hikaru Ikeda[c], Masaru Takagi[d], Masamichi Nishio[d], Masaaki Satoh[e], Shigeo Nakamura[f], Hidetoshi Satoh[g], Masato Hareyama[a]

[a]*Department of Radiology, Sapporo Medical University, School of Medicine, Japan,* [b]*Department of Radiation Oncology, Aichi Cancer Center, Japan,* [c]*Department of Radiology, Sapporo City Hospital, Japan,* [d]*Department of Radiology, National Sapporo Hospital, Japan,* [e]*Department of Clinical Pathology, Sapporo Medical University, School of Medicine, Japan,* [f]*Department of Clinical Pathology, Aichi Cancer Center, Japan,* [g]*Department of Clinical Pathology, Sapporo City Hospital, Japan*

Abstract

***Background and purpose*:** This study was conducted to analyze the influence of radiotherapy doses and chemotherapy doses and clinical parameters on in-field disease control in order to assess the optimal radiation doses for treatment of mature T/NK-cell lymphomas according to the newly proposed WHO classification.

***Patients and methods*:** Subjects consisted of 62 patients with mature T/NK-cell lymphomas treated with radiotherapy at four Japanese institutions between 1983 and 2002. We reevaluated all histopathological specimens of non-Hodgkin's lymphomas (NHL), using the WHO classification. Radiation therapy was usually delivered to the involved field. The majority of patients also received adriamycin-based chemotherapy such as CHOP, modified CHOP, or more intensive chemotherapy.

***Results*:** There were no significant differences in radiosensitivity among subtypes of mature T/NK-cell lymphomas, at least between extranodal NK/T-cell lymphomas, nasal type and peripheral T-cell lymphomas, unspecified. There was a radiation dose-response in non-bulky mature T/NK-cell lymphomas, indicating that radiation doses of more than 52 Gy may be required to obtain in-field control. However, it was difficult to obtain local control of bulky T-cell lymphomas, even with high doses of irradiation.

***Conclusions*:** Mature T/NK-cell lymphomas were more radioresistant than B-cell lymphomas such as diffuse large B-cell lymphomas (DLBCL). The chemotherapy including adriamycin did not improve the in-field control of mature T/NK-cell lymphomas. These results were obtained by using non-randomized data and the significance of these results is limited by bias in data. However, our results suggest that the treatment strategy which is usually used for DLBCL, that is, a combined modality of CHOP and around 40 Gy of radiotherapy, may not be sufficiently effective for mature T/NK-cell lymphomas.
 Radiotherapy and Oncology 79 (2006) 179-184.

Keywords: Non-Hodgkin's lymphoma; Mature T/NK-cell lymphoma; WHO classification; Radiation dose-response; In-field control

T-cell non-Hodgkin's lymphomas (NHL) are rare in Europe and the United States, where they constitute about 15-20% of aggressive lymphomas [1,2]. They are more common in Taiwan and Japan [3,4]. Mature T/NK-cell lymphomas makes up the majority of T-cell NHL in adult patients. Mature T/NK-cell lymphomas has been reported to have poor prognosis in most series [2,3,5-7]. However, regarding standardization of treatment, classification, and pathophysiology of mature T/NK-cell lymphomas the current knowledge is markedly behind that of B-cell lymphomas, which are approximately 10 times more frequent [8].

Advances in immunophenotyping and molecular genetics have identified T-cell NHL not identified by the Working Formulation. These entities have been included in the Revised European-American Lymphoma (REAL) and subsequent WHO classifications [9,10], which use a combination of morphologic, immunologic, genetic and clinical information to define distinct disease entities. These classifications allow for the identification of subgroups of patients with T-cell lymphomas but are not based on patient outcome. Only a few previous studies have evaluated mature T/NK-cell lymphomas in relation to the REAL or WHO classifications [11].

In particular, no information is available on the optimal radiotherapy dose necessary to achieve in-field disease control in patients with mature T/NK-cell lymphomas who

0167-8140/$ - see front matter doi:10.1016/j.radonc.2006.03.014

are treated with combined chemotherapy and radiotherapy. Patient numbers within each lymphoma subtype were small, reflecting the rarity of mature T/NK-cell lymphomas in clinical practice, and a larger series would be improbable in a single center. Small numbers within each subtype also precluded a more detailed analysis of different treatment types. Therefore, the accumulated experiences of various institutions should be utilized to obtain a more effective treatment for this tumor.

This report is a multi-institutional study of patients with mature T/NK-cell lymphomas, which were treated with radiotherapy and chemotherapy at four hospitals in Japan between 1983 and 2002. We reevaluated histopathological specimens of NHL, using the WHO classification and investigated the relationship between the clinical characteristics and histopathological classification of these specimens. Then, we analyzed the influence of radiotherapy doses as well as chemotherapy on in-field disease control in order to assess the optimal radiation doses for treatment of mature T/NK-cell lymphomas according to the WHO classification.

Materials and methods

Patient characteristics

There were 68 patients with mature T/NK-cell lymphomas treated with radiotherapy at Sapporo Medical University Hospital, Aichi Cancer Center, Sapporo City Hospital, and National Sapporo Hospital between 1983 and 2002. Six patients were excluded from this study because their irradiation was aborted due to various reasons before the planned dose was reached.

Malignant lymphomas with histologic features other than mycosis fungoides were accepted as mature T/NK-cell lymphomas when a T/NK-cell phenotype was demonstrated and/or by the presence of T/NK-cell receptor clonality. Primary brain lymphomas were excluded from this study because their natural history and prognosis are very different from the other lymphomas [12].

The characteristics of mature T/NK-cell lymphomas patients are summarized in Table 1. There were 26 extranodal NK/T-cell lymphomas, nasal type (nasal NK/T-cell lymphoma), 23 peripheral T-cell lymphomas, unspecified (peripheral T lymphoma, unspec.), eight anaplastic large-cell lymphomas, T/null cell type, two adult T-cell leukemia/lymphoma, two angioimmunoblastic T-cell lymphoma, and one enteropathy-type T-cell lymphoma. Nasal NK/T-cell lymphoma is more prevalent in the younger generation, compared with the other mature T/NK-cell lymphomas.

Table 2 shows the histopathological distribution according to primary sites. All but one patient with nasal NK/T-cell lymphoma were seen only in the nasal sinus. However, peripheral T lymphoma, unspec., and anaplastic large-cell lymphomas had originations in various primary sites.

Histology and T/B phenotype

Three of the authors (M.S., E.N., H.S.) reassessed specimens using the morphologic and immunological techniques described below. Histological classification was performed according to the WHO classification [10]. Immunohistochemical studies were performed using paraffin sections, the avidin-biotin peroxidase complex technique, and a panel of monoclonal antibodies (L2 CD3, MT1, UCHL1, and CD56).

Treatment

Radiation therapy was usually delivered to the involved field. In patients treated with chemotherapy and subsequent radiotherapy, the radiation field was set for primary sizes of lesions. The dose per fraction ranged from 1.8 to 2.0 Gy. All treatment regimens included five daily fractions per week. The standard total radiation doses were 40-50 Gy. Four patients who were treated before 1985 received less than 40 Gy. Radiation was added in excess of 50 Gy when irradiated tumors did not disappear at the originally intended dose. CT has been used to examine the extent of tumor invasion in all patients and MRI also has been used since 1988. We checked simulator films or dose distributions

Table 1
Characteristics of the patients

	Nasal NK/T-cell L	Peripheral T L, unspec.	Anaplastic large-cell L
Male:female	17:9	11:12	2:6
Age (average)	27-74 (48)	33-75 (57)	24-75 (56)
Radiation dose (Gy)			
Median	50	44	44.6
Range	30-78	39-64	30-54.6
Chemotherapy			
None, or regime not including ADM	4	5	2
CHOP, modified CHOP or more intensive	14	15	6
Regime including platium-based drug	6	1	0
High dose chemo+PBSCT	2	2	0
Stage I	18	14	3
Stage II	5	5	3
Stage III or IV	3	4	2

L, lymphoma; DLBCL, diffuse large B-cell lymphoma; PBSCT, peripheral blood stem cell transplantation.

Table 2
Primary sites and pathological classification

Pathology	Orbit	NC	WR	Skin	L/N	Others
Peripheral T/NK-cell L	1	7	2	4	7	2
Nasal NK/T-cell L		25	1			
Anaplastic large-cell L		2	1	1	3	1
Angioimmunoblastic L			1		2	
Adult T-cell L			1	2		

NC, nasal cavity; WR, Waldeyer's ring; L/N, lymph nodes.

data in all patients and made sure there were no geographical misses. The conformal radiotherapy techniques using multi-leaf collimators has been used since 1985 to reduce doses to critical normal structures (Table 1).

Chemotherapy has been changed according to era. Chemotherapy was not used or regime not including adriamycin (ADM) was used from 1980 to 1985. CHOP had been used since 1985 until 2000. Regime including platium-based drugs have been performed since 1993. Peripheral blood stem cell transplantation (PBSCT) was introduced to advanced disease such as stage III or IV at 1998. Such change reflects the lack of chemotherapy regime, which is effective to T/NK-cell lymphomas.

We classified chemotherapy into four categories, namely: 'none, or regime not including ADM', 'CHOP, modified CHOP or more intensive', 'regime including platium-based drugs', and 'high dose chemotherapy + PBSCT'.

The greatest number of patients received CHOP (cyclophosphamide: 750 or 600 mg/m^2 in the elderly; adriamycin: 50 or 40 mg/m^2 in the elderly; vincristine: 1.4 mg/m^2; and prednisolone: 60 mg$\times$5 days), modified CHOP, or more intensive chemotherapy, mostly before radiotherapy.

The third category, 'regime including platium-based drugs', included DeVIC (dexamethasone 40 mg/m$^2\times$3 days, etoposide 100 mg/m$^2\times$3 days, ifosphamide 1500 mg/m$^2\times$3 days, and carboplatin 300 mg/m$^2\times$3 days). This kind of chemotherapy has recently been used for nasal NK/T-cell lymphoma.

Statistical analysis

The overall survival rates and distant involvement-free survival rates were calculated from the start of treatment by the Kaplan-Meier method, and differences in the survival rates were examined by the log-rank test. The median follow-up for the living patients was 61 months.

In-field failure was defined as any failure with an in-field component; that is, any recurrence in the irradiated volume. In this study to examine the relationship between dose versus in-field control, all patients were included regardless of the disease stage. The living patients whose follow up periods were less than 24 months were excluded from this analysis although they had achieved local control.

Results

The overall five-year survival rate for stage I or II patients with peripheral T lymphoma, unspec. was 84% and that with NK/T-cell lymphoma was 62%. The distant-involvement-free five-year survival rate for stage I or II patients with peripheral T lymphoma, unspec. was 85% and that with NK/T-cell lymphoma was 62%. NK/T-cell lymphoma appeared to the worse prognosis than peripheral T lymphoma, unspec., but there were no significant differences in the overall survival rate and distant-involvement-free survival rate.

There were 20 patients with mature T/NK-cell lymphomas who were treated with chemotherapy before radiation. After chemotherapy, 12 patients obtained CR, three PR, three NC, and two PD. In-field recurrences were seen in 3 of 12 patients with CR, none of three PR, all three NC, and all three PD.

Fig. 1a demonstrates the in-field local control of nasal NK/T-cell lymphoma according to intensity of chemotherapy and dose of radiotherapy. The intensity of chemotherapy was represented by doses of ADM. The patients treated with a regime including platium-based drugs or high dose chemotherapy + PBSCT are separately demonstrated in the vertical axis. The patients with bulky mass ($>$6 cm in diameter) were also separately demonstrated. Twenty five patients with nasal NK/T-cell lymphoma were included in this analysis. One patient with bulky tumor was excluded from this analysis due to short follow-up period. Ten patients had bulky tumor and the other 15 patients had non-bulky tumor. In non-bulky tumors, there was a relationship between radiation dose and in-field control. Only three of the nine patients who were treated with 52 Gy or less had local control whereas all six patients who were treated with more than 54 Gy obtained local control. The dose of ADM or chemotherapy with platium-based drugs had no influence on in-field control of nasal NK/T-cell lymphoma. In bulky tumors, there was no apparent relationship between radiation dose and in-field control, suggesting that it was very difficult to obtain local control of nasal NK/T-cell lymphoma that was larger than 6 cm in diameter.

Fig. 1b demonstrates the in-field local control of peripheral T lymphoma, unspec. according to intensity of chemotherapy and dose of radiotherapy. The total of 23 patients with peripheral T lymphoma and 26 tumors were included in this analysis. There were only two tumors, which were bulky in this analysis. In non-bulky tumors, there was a relationship between radiation dose and in-field control. Only 9 of the 16 patients who were treated with 46 Gy or less had local control whereas five of six patients who were treated with more than 48 Gy achieved local control. The dose of adriamycin had no influence on local control of peripheral T lymphoma, unspec.

In addition to patients with nasal NK/T-cell lymphoma and peripheral T lymphoma, unspec., four patients with non-bulky tumors of other histologies were also evaluable for in-field control. A patient with adult T-cell leukemia/lymphoma treated with 44 Gy of radiotherapy alone underwent in-field recurrence. All two patients with anaplastic large-cell lymphoma had in-field control, who were treated with 51 Gy of radiotherapy alone or 54.6 Gy of radiotherapy and